# Supporting Information

## Oxygen spillover from $RuO_2$ to $MoO_3$ enhances activity and durability of $RuO_2$ for acidic oxygen evolution

Wangyan Gou, ‡[abc] Shishi Zhang,‡[d] Yichen Wang,[b] Xiaohe Tan,[ab] Linqing Liao,[ab] Zening Qi,[e] Min Xie,[e] Yuanyuan Ma,*[ab] Yaqiong Su*[d] and Yongquan Qu*[b]

[a] *Research & Development Institute of Northwestern Polytechnical University in Shenzhen, Shenzhen 518057, Guangdong, China*

[b] *Key Laboratory of Special Functional and Smart Polymer Materials of Ministry of Industry and Information Technology, School of Chemistry and Chemical Engineering, Northwestern Polytechnical University, Xi'an, 710072, China*

[c] *School of Materials Engineering, Xi'an Aeronautical University, Xi'an, 710077, China*

[d] *School of Chemistry, Engineering Research Center of Energy Storage Materials and Devices of Ministry of Education, National Innovation Platform (Center) for Industry-Education Integration of Energy Storage Technology, Xi'an Jiaotong University, Xi'an, 710049, China*

[e] *Xi'an Yiwei Putai Environmental Protection co., LTD, Xi'an, 710075, China*

‡*These authors contributed equally to this work.*

Correspondence and requests for materials should be addressed to yyma@nwpu.edu.cn; yqsu1989@xjtu.edu.cn; yongquan@nwpu.edu.cn

## Experimental Section

### Chemicals and materials

Poly(vinyl pyrrolidone) (PVP, $M_W$=1300000), ruthenium chloride hydrate ($RuCl_3 \cdot 3H_2O$, 99.9%), commercial rutile-type $RuO_2$ (99.9%), 5 *wt.* % Nafion solution, and ammonium molybdate ($(NH_4)_2MoO_4 \cdot 4H_2O$, 99.9%) were purchased from Sigma-Aldrich. *N, N*-dimethylformamide (DMF) and sulfuric acid ($H_2SO_4$) were obtained from Energy Chemical. All chemicals were used as received without any further purification. Ultrapure water (18.2 MΩ $cm^{-1}$) used in the experiments was supplied by a Millipore System (Millipore Q).

### Synthesis of $RuO_2/MoO_3$ nanowires

$RuO_2/MoO_3$ nanowires were synthesized through the electrospinning and subsequent calcination at various temperatures. In a typical process of $RuO_2/MoO_3$ synthesis, 400 mg of PVP was dissolved in 1.8 mL of DMF under a mechanical stirring of 6 h. Meanwhile, $RuCl_3 \cdot 3H_2O$ (0.34 mmol) and $(NH_4)_2MoO_4 \cdot 4H_2O$ (0.06 mmol) were dissolved in 0.7 mL DMF and 0.5 mL $H_2O$ under ultrasonication, respectively. The total molar amount of (Ru + Mo) was fixed at 0.4 mmol. The solution of $RuCl_3 \cdot 3H_2O$ was dripped into as-prepared PVP solution under stirring, and then the $(NH_4)_2MoO_4 \cdot 4H_2O$ solution was dripped into the preceding mixture and stirred for 6 h to obtain a homogeneous sol. After 2 h of reposing, as-prepared sol was electrospun by a self-built electrospinning system with ejecting at a flow rate of 3 μL $min^{-1}$ in a plastic syringe from an injection pump. The distance between the metal needle and aluminum foil was fixed at 15 cm. The applied electric voltage was 13 kV. Afterwards, the electrospun nanofibers were collected into a quartz tube, calcinated at the desired temperatures for 6 h in air with a ramping rate of 3 °C $min^{-1}$. After cooling to room temperature, the resulting black products were named as $RuO_2/MoO_3$.

### Characterizations

Transmission electron microscope (TEM, JEOL JEM2100) and scanning TEM (STEM, FEI Talos F200X) with energy dispersive X-ray (EDX) spectroscopy were used to examine the morphology and elemental distribution of as-prepared catalysts. The X-ray

diffraction (XRD) was performed on a Shimadzu diffractometer using a Cu K source (λ=0.1541 nm) at 30 kV and 20 mA. The X-ray photoelectron spectroscopy (XPS) was performed on a PHI 1600 equipped with Al Kα radiation. All binding energies were referenced to the C 1s peak (284.8 eV) arising from the adventitious carbon-containing species. Metal element dissolution was analyzed using a PerkinElmer NexION 300X Inductively coupled plasma mass spectrometer (ICP-MS).

**Oxygen Temperature Programmed Desorption ($O_2$-TPD)**

The samples (50 mg) were first pre-treated with Ar (50 mL $min^{-1}$) from room temperature to 300 °C at a rate of 10 °C $min^{-1}$. They were kept at 300 °C for 30 minutes and then cooled to 40 °C at 10 °C $min^{-1}$. Subsequently, a mixture of 6% $O_2$ in He (50 mL $min^{-1}$) was introduced into the system and kept at 40 °C for 60 min. Finally, the samples were treated with pure Ar (50 mL $min^{-1}$) to stabilize the baselines and then heated up to 790 °C at 10 °C $min^{-1}$ to start $O_2$ desorption process.

**Electrochemical Measurements**

The catalyst ink was prepared in the following method. Firstly, 4 mg of various catalysts was added into 1 mL solution consisting of 768 μL of water, 200 μL of ethanol, 32 μL of 5 *wt.*% Nafion solution and ultrasonically dispersed for 30 min. Then, 10 μL of the catalyst ink was loaded onto a piece of carbon paper (CP, surface area of 0.071 $cm^{-2}$) and dried naturally. The electrochemical performance without IR compensation was carried out using a typical three-electrode setup on a CHI 760E electrochemical workstation (CH Instruments, Shanghai, China). The evaluation of catalytic performance was measured in a three-electrode system with the catalyst coated CP as the working electrode, the graphite rod as the counter electrode and Ag/AgCl with the saturated KCl filling solution electrode as the reference electrode in 0.5 M $H_2SO_4$ aqueous solution. The electrolyte was degassed with a flow of Ar for 30 min to remove the dissolved oxygen before the electrochemical measurements. The catalytic activity of various catalysts was evaluated by linear scanning voltammetry (LSV) at the desired scan rates. All the potentials were calibrated to the reversible hydrogen electrode (RHE) by using equation: E(RHE) = E(Ag/AgCl) + 0.0591*pH + 0.196. The polarization curves were plotted as the potential versus the log current (log[i]) to obtain

the Tafel plots. The Tafel slope (b) was obtained by fitting the linear portion of the Tafel plots to the Tafel equation (η = b log[i]+a). To investigate the stability, chronopotentiometry (CP) were performed at a current density of 10 mA $cm^{-2}$. Cyclic voltammograms (CVs) were recorded in the potential range of 0.1-1.6 V *vs.* RHE at a scan rate of 50 mV $s^{-1}$. The electrochemical impedance spectra (EIS) were measured at a voltage of 1.41 V *vs.* RHE in the frequency range of 100 kHz to 0.1 Hz on an Autolab PGSTAT204 potentiostat.

**Electrochemical active surface area (ECSA)**

To determine the ECSA of various electrocatalysts, a series of cyclic voltammetry (CV) curves were recorded at various scan rates (10, 20, 30, 40, 50 and 60 mV $s^{-1}$) within the potential window between 0.99 and 1.09 V *vs.* RHE. The geometric double layer capacitance ($C_{dl}$) was calculated by plotting the difference of current density $\Delta J = J_{anodic} - J_{cathodic}$ at 1.04 V *vs.* RHE against the scan rates, and the slope of the linear trend was twice of $C_{dl}$.

Finally, the ECSA of catalyst was estimated according to the Eq. (1):

$$ECSA = \frac{C_{dl}}{C_s} \times ASA \quad (1)$$

where $C_s$ was the specific capacitance of the sample, and ASA was the actual surface area of the electrode. In this work, the value of $C_s$ was estimated to be 0.06 mF $cm^{-2}$. The current density $j_{ECSA}$ (mA $cm_{ECSA}^{-2}$) value was normalized with the effective electrochemical active surface area (ECSA) from Eq. (2):

$$j_{ECSA} = \frac{i \times 1000}{ECSA} \quad (2)$$

where i (A) was the current and ECSA was the effective electrochemical active surface area.[1]

**Apparent activation energy ($E_a$)**

To extract the apparent activation energy for the acidic OER, the electrochemical measurements of various electrocatalysts were conducted in 0.5 M $H_2SO_4$ solution at different temperatures. For the heterogeneous electrocatalytic reaction, the exchange

current density ($j_0$) can be expressed from the apparent activation energy ($E_a$) in the Arrhenius Eq. (3):

$$j_0 = Aexp(-\frac{E_a}{RT}) \quad (3)$$

where A is the apparent pre-exponential factor, R is the ideal gas constant (8.314 J $K^{-1}$ $mol^{-1}$), T is the temperature in Kelvin (K). Therefore, $E_a$ can be further calculated by fitting the slope of the Arrhenius plot using Eq. (4):

$$\left|\frac{\partial(lg_{10}j_0)}{\partial(1/T)}\right| = -\frac{E_a}{2.303R} \quad (4)$$

while the intercept of $lg\, j_0$ *vs.* 1/T plot is the logarithm of A.[2]

**Operando Fourier transformed infrared (FTIR) measurements**

Operando electrochemical FTIR investigations were carried out on a NICOLET iS50 FTIR infrared spectrometer equipped with an MCT/B detector, which was cooled by liquid nitrogen. The catalyst inks were dropped and dried on carbon papers. Ag/AgCl electrode and graphite rod were used as the reference and counter electrodes, respectively. The electrode potential was held at open circuit potential (OCP) in 0.5 M $H_2SO_4$ and a background spectrum was recorded. The applied electrode potentials were increased from 1.2 V to 1.6 V stepwise. Meanwhile, the infrared spectra at various applied potentials were recorded in a range of 650~4000 $cm^{-1}$ at a resolution of 4 $cm^{-1}$ and 32 scans per spectrum.[3]

**Operando differential electrochemical mass spectroscopy (DEMS) with isotope labelling**

Operando DEMS with isotope labelling data ($^{18}$O-DEMS) was collected on a DEMS Spectrometer QAS100 (SEM detector, EI ion source, 70 eV). The measurements were performed in a setup of two interconnected vacuum chambers including a mass spectrometer chamber with a high vacuum and a second chamber with a mild vacuum. The electrochemical cell was directly connected with the second chamber. Due to the pressure difference between two chambers, the *in situ* generated oxygen would not be released upward into the air and indeed was drawn downward into the vacuum chamber

for mass spectrometer analysis. The catalyst inks were directly dropped onto an Au electrode (Au film sputtered on a porous polytetrafluoroethylene membrane) as the working electrode. For a typical measurement, aqueous $H_2SO_4$ (0.5 M) with $H_2{}^{18}O$ as solvent was employed as the electrolyte. Before the electrochemical measurements, the electrolytes were purged with high-purity Ar to remove the dissolved oxygen. For isotope labelling studies, the catalysts including $RuO_2/MoO_3$ and $RuO_2$ were subjected to five consecutive CV cycles (the potential window of 0.98~1.72 V *vs.* RHE at a scan rate of 5 mV $s^{-1}$) for labelling the catalyst surface with $^{18}O$. The mass signals of the gaseous products $^{32}O_2$, $^{34}O_2$ and $^{36}O_2$ were monitored simultaneously. Then the catalysts were washed thoroughly with Millipore Q water ($H_2{}^{16}O$) to remove the physically attached $H_2{}^{18}O$ molecules on the catalyst surface. While, the $^{18}O$-lattice oxygen species that chemically bonded on the catalyst surface remained. The isotope-labelled catalysts then operated in 0.5 M $H_2SO_4$ electrolyte with $H_2{}^{16}O$ as the solvent. Afterwards, the mass signals of the gaseous products $^{32}O_2$, $^{34}O_2$ and $^{36}O_2$ were monitored by the mass spectrometer through the identical operation.[4]

## Computational section

The spin-polarized calculations within the density functional theory (DFT) framework were carried out by the Vienna *ab initio* simulation package (VASP).[5] The interactions between core and electrons were represented by the projector-augmented wave (PAW) method and the generalized gradient approximation (GGA) with the Perdew-Burke-Ernzerhof (PBE) exchange-correlation functional.[6,7] The Brillouin-zone integrations were performed using a (2×2×1) Monkhorst-Pack mesh. The iterative process considered was convergences, when the force on the atom was < 0.05 eV $Å^{-1}$ and the energy change was < $10^{-4}$ eV per atom. In this work, an implicit solvent model was considered for the effects of water solvent environment.[8]

The $RuO_2$(110) and $MoO_3$(021) surfaces were modeled with a slab of four atomic layers in which the bottom two layers were frozen, and a vacuum layer of about 15 Å along the z-axis was built. In addition, the surface of $RuO_2$(110) was covered by oxygen (*O), which shows high activity.[9] For $MoO_3$/ $RuO_2$, one atomic layer of $MoO_3$ was

loaded on the O-coverage $RuO_2$(110) surface.

The Gibbs free energies (G) at 298.15 K and 1 atm were calculated by Eq. (5):

$$G = H - TS = E_{DFT} + E_{ZPE} + \int_0^{298.15\ K} C_V dT - TS \quad (5)$$

where $E_{DFT}$ is the total energy obtained from DFT optimization, $E_{ZPE}$ is the zero-point vibrational energy using the harmonic approximation, $C_V$ is the heat capacity, $T$ is the kelvin temperature, and $S$ is the entropy.[10] The entropy of $H_2$ was taken from NIST database. And the free energy of liquid water was calculated as an ideal gas at 3534 Pa, which corresponds to the vapor pressure of water.[11] The computational hydrogen electrode (CHE) model was used to calculate the free energy of electrocatalytic OER.[12]

To evaluate the stability of the activity of O atoms, the formation energies ($G_{f\text{-}vacancy}$) of oxygen vacancies were proposed by DFT calculation and followed the Eq. (6):

$$G_{f-vacancy} = G_{vacancy} + G_O - G_{perfect} \quad (6)$$

where $G_{perfect}$ represents the energy of the perfect compounds, $G_{vacancy}$ is the energy of compounds with a O vacancy, $G_O$ is the energy of an O atom.

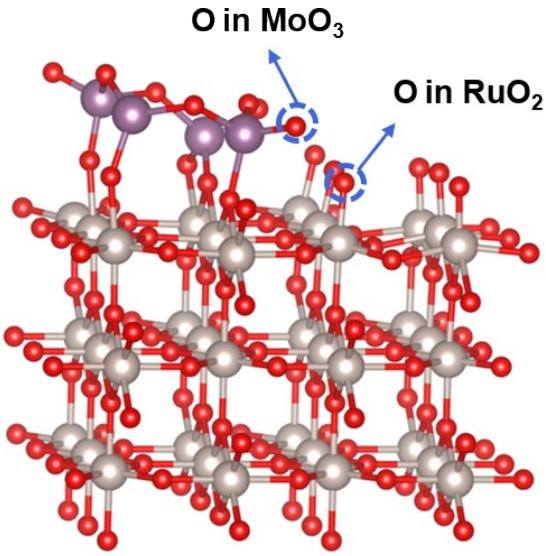


**Fig. S1.** Heterojunction structure model of $RuO_2$ and $MoO_3$.

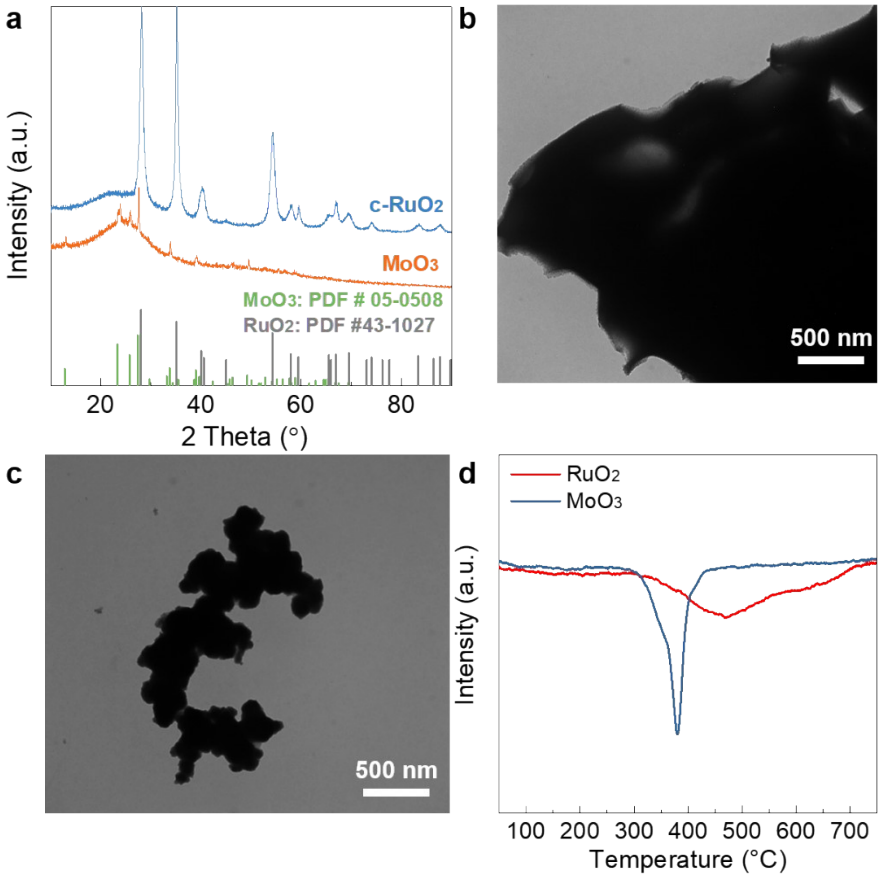


**Fig. S2.** (a) XRD patterns of $MoO_3$ and commercial $RuO_2$. (b) TEM image of $MoO_3$. (c) TEM image of c-$RuO_2$. (d) TPD profiles of $RuO_2$ and $MoO_3$.

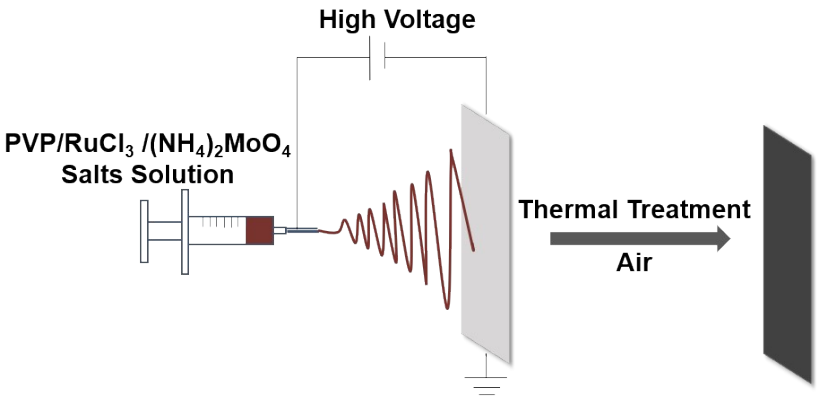


**Fig. S3.** Schematic illustration of the synthetic approach of $RuO_2/MoO_3$.

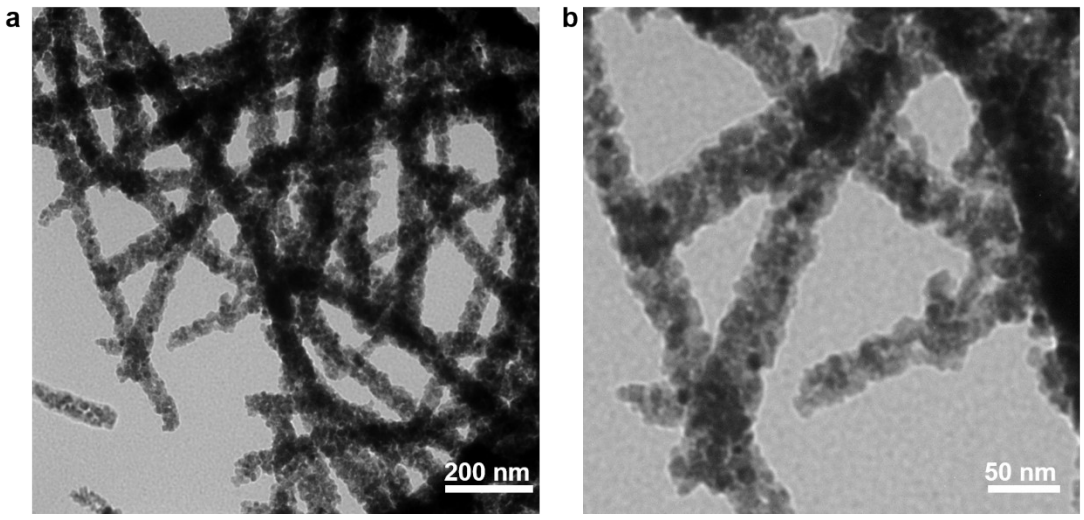


**Fig. S4.** TEM images of $RuO_2$ nanowire synthesized through the identical approach of $RuO_2/MoO_3$ in the absence of Mo precursor. The calcination temperature was 350 °C.

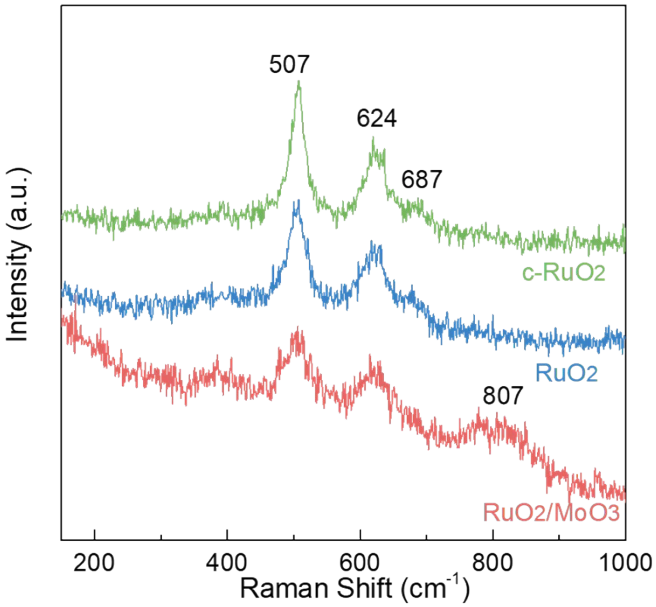


**Fig. S5.** Raman spectra of $RuO_2/MoO_3$, $RuO_2$ and c-$RuO_2$.

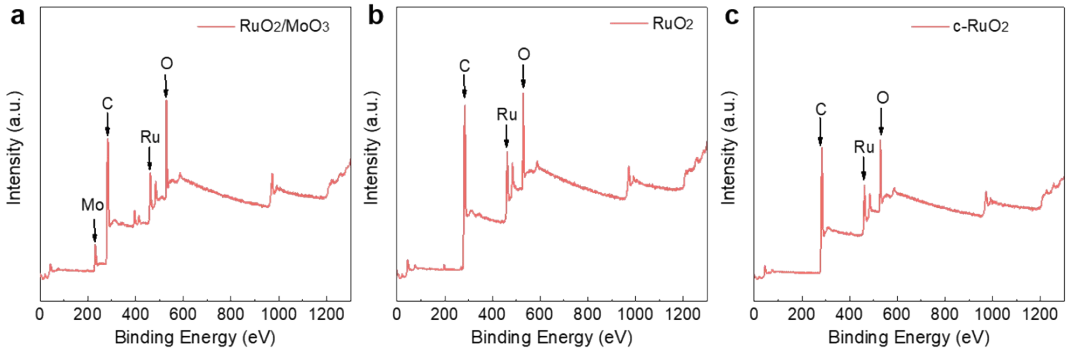


**Fig. S6.** Full XPS spectra (a) $RuO_2/MoO_3$, (b) $RuO_2$, (c) c-$RuO_2$.

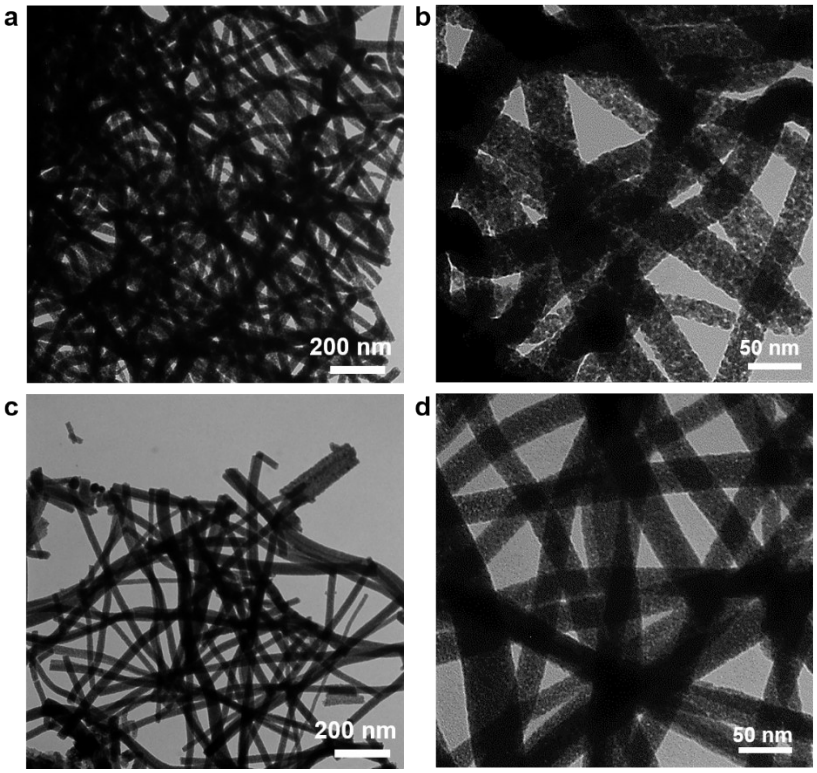


**Fig. S7.** Low and high magnification TEM images of $RuO_2/MoO_3$-x (x represents the molar fraction of Mo in the electrocatalysts): (a-b) $RuO_2/MoO_3$-10%; (c-d) $RuO_2/MoO_3$-20%. The calcination temperature was 350 °C.

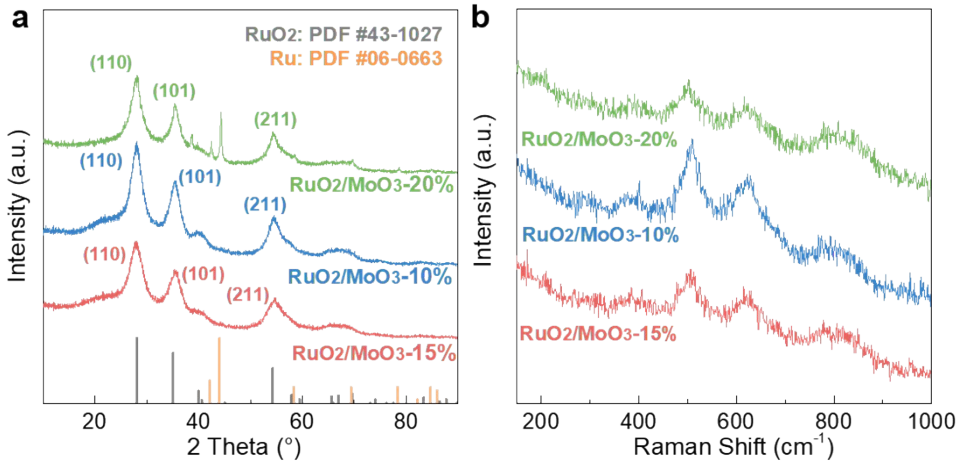


**Fig. S8.** (a) XRD patterns and (b) Raman spectra for $RuO_2/MoO_3$-10%, $RuO_2/MoO_3$-15%, and $RuO_2/MoO_3$-20%. The calcination temperature was 350 °C.

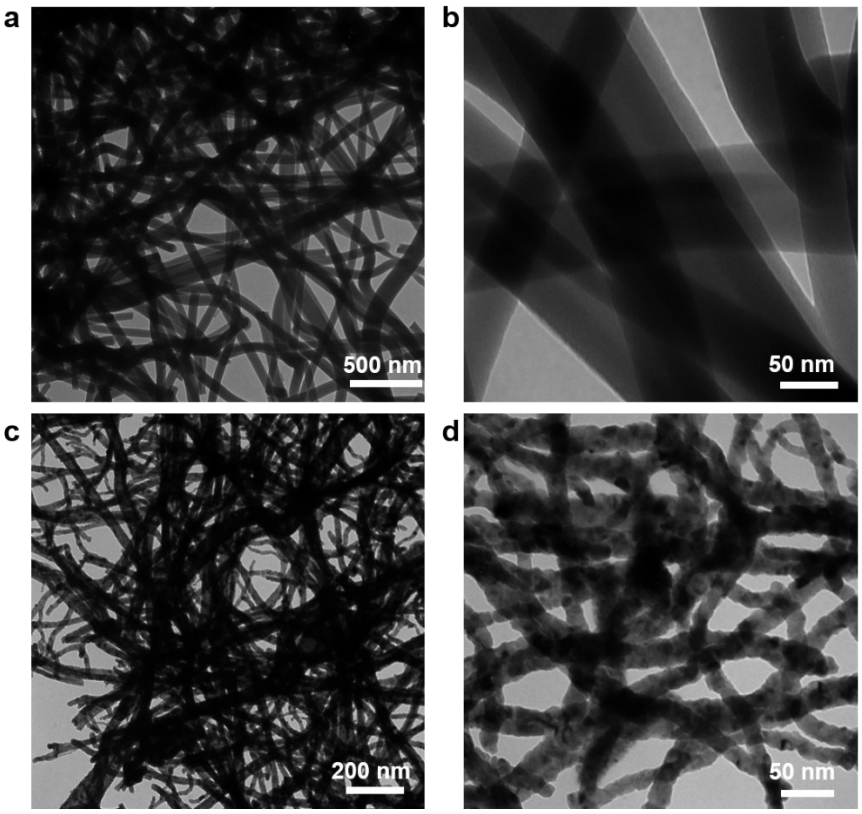


**Fig. S9.** Low and high magnification TEM images of $RuO_2/MoO_3$-T (T represents the calcination temperature): (a-b) $RuO_2/MoO_3$-250; (c-d) $RuO_2/MoO_3$-450. The molar ratio of Ru: Mo was 85:15.

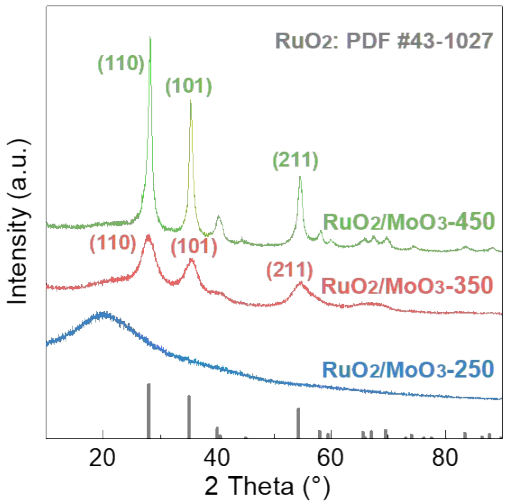


**Fig. S10.** XRD patterns for $RuO_2/MoO_3$-250, $RuO_2/MoO_3$-350, and $RuO_2/MoO_3$-450. The molar ratio of Ru: Mo was 85:15.

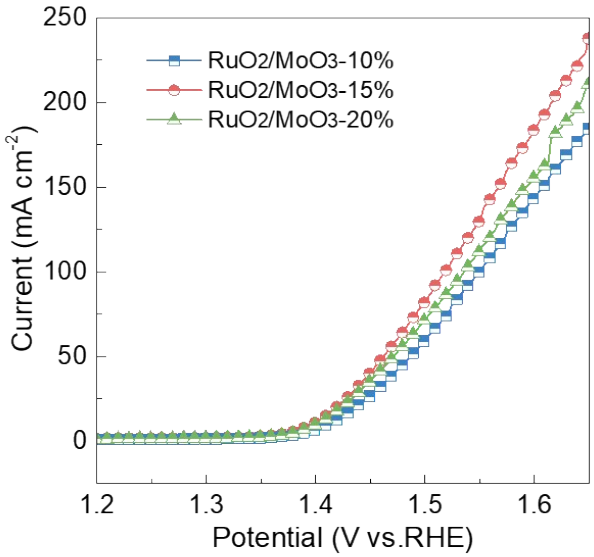


**Fig. S11.** LSV curves of $RuO_2/MoO_3$-10%, $RuO_2/MoO_3$-15%, and $RuO_2/MoO_3$-20%. The calcination temperature was 350 °C.

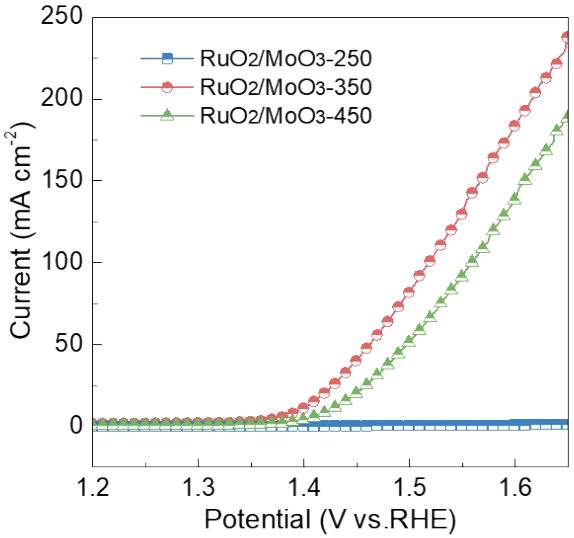


**Fig. S12.** LSV curves of $RuO_2/MoO_3$-250, $RuO_2/MoO_3$-350, and $RuO_2/MoO_3$-450. The molar ratio of Ru: Mo was 85:15.

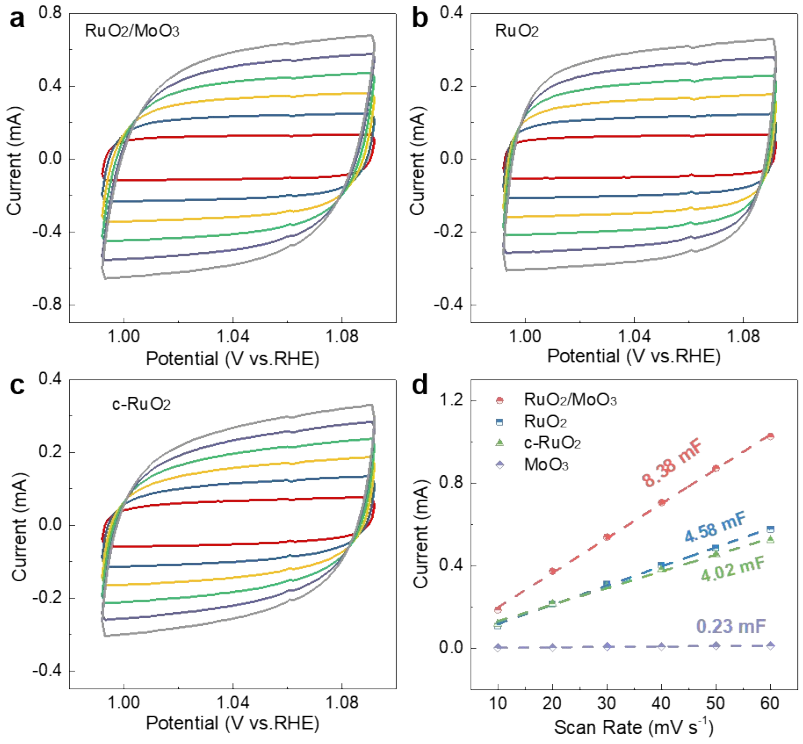


**Fig. S13.** CV curves of (a) $RuO_2/MoO_3$, (b) $RuO_2$, (c) c-$RuO_2$. (d) Linear fitting of the capacitive currents versus CV scan rates and double layer capacitance values ($C_{DL}$) for $RuO_2/MoO_3$, $RuO_2$, c-$RuO_2$, and $MoO_3$ catalysts.

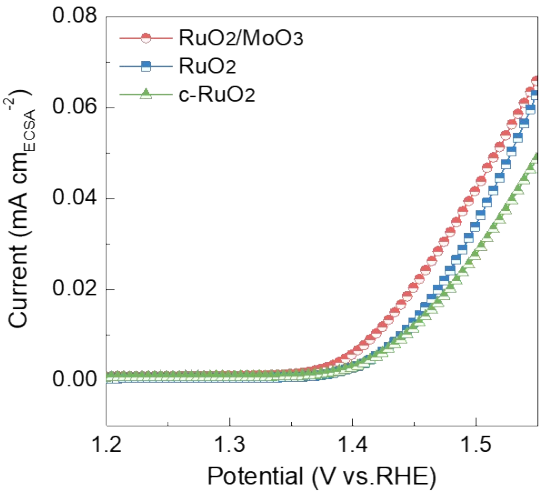


**Fig. S14.** LSV curves of $RuO_2/MoO_3$, $RuO_2$, c-$RuO_2$, normalized by effective electrochemical surface areas (ECSA).

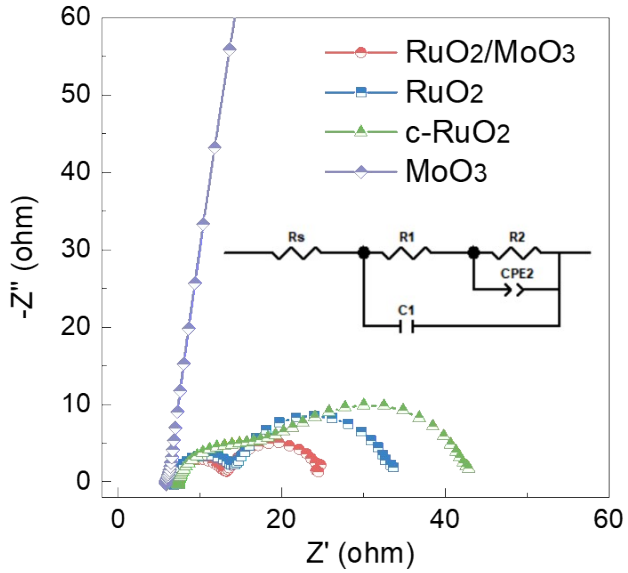


**Fig. S15.** EIS Nyquist plots of $RuO_2/MoO_3$, $RuO_2$, c-$RuO_2$ and $MoO_3$ catalysts recorded at an OER potential of 1.41 V *vs.* RHE. The inset represented simulated equivalent circuit.

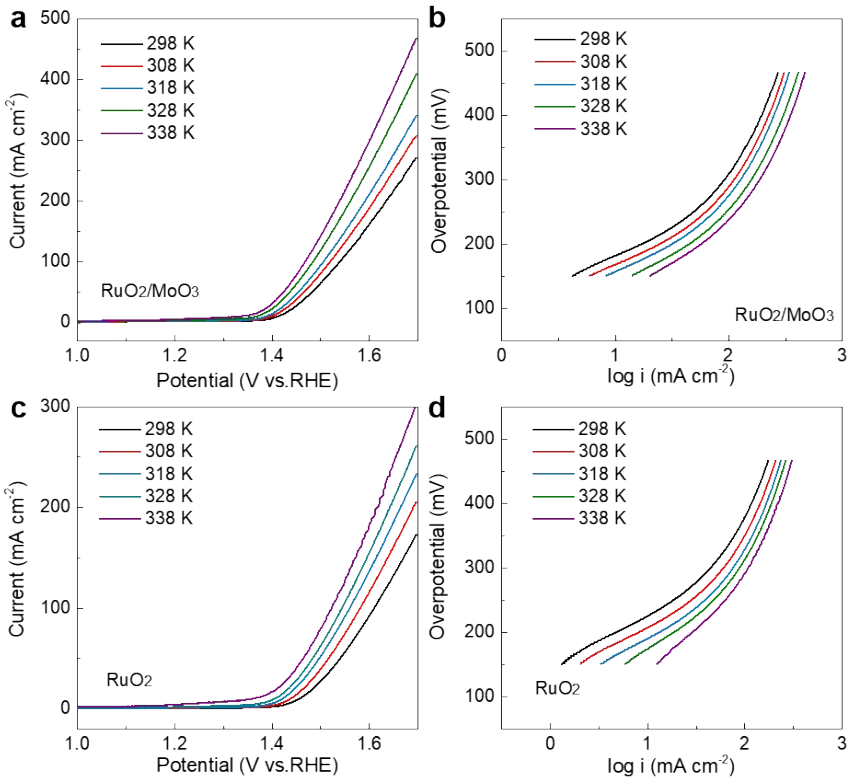


**Fig. S16.** LSV curves and derived Tafel plots of (a, b) $RuO_2/MoO_3$ and (c, d) $RuO_2$ at different temperatures.

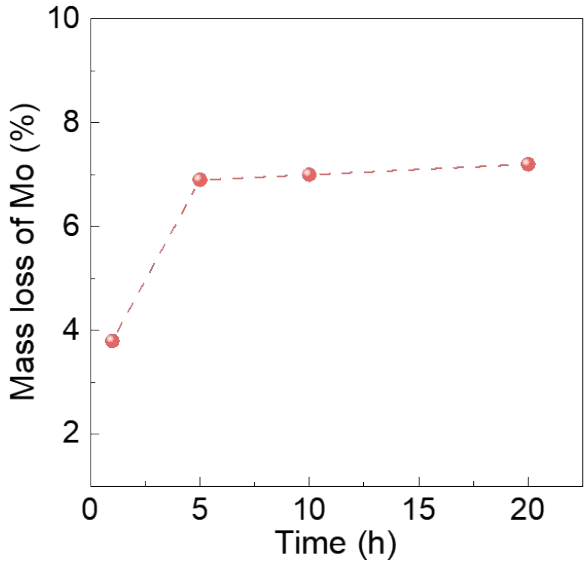


**Fig. S17.** The weight percentage of mass loss for Mo in $RuO_2/MoO_3$ during stability test.

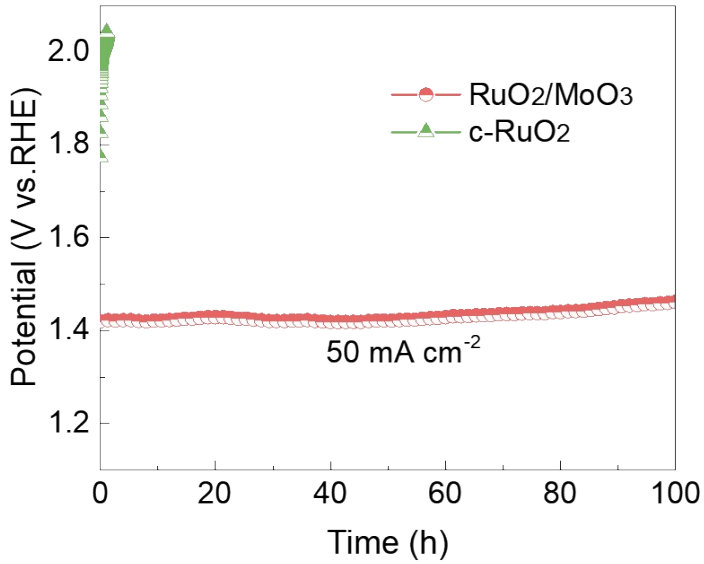


**Fig. S18.** Chronopotentiometry tests at a current density of 50 mA $cm^{-2}$ for $RuO_2/MoO_3$ and c-$RuO_2$.

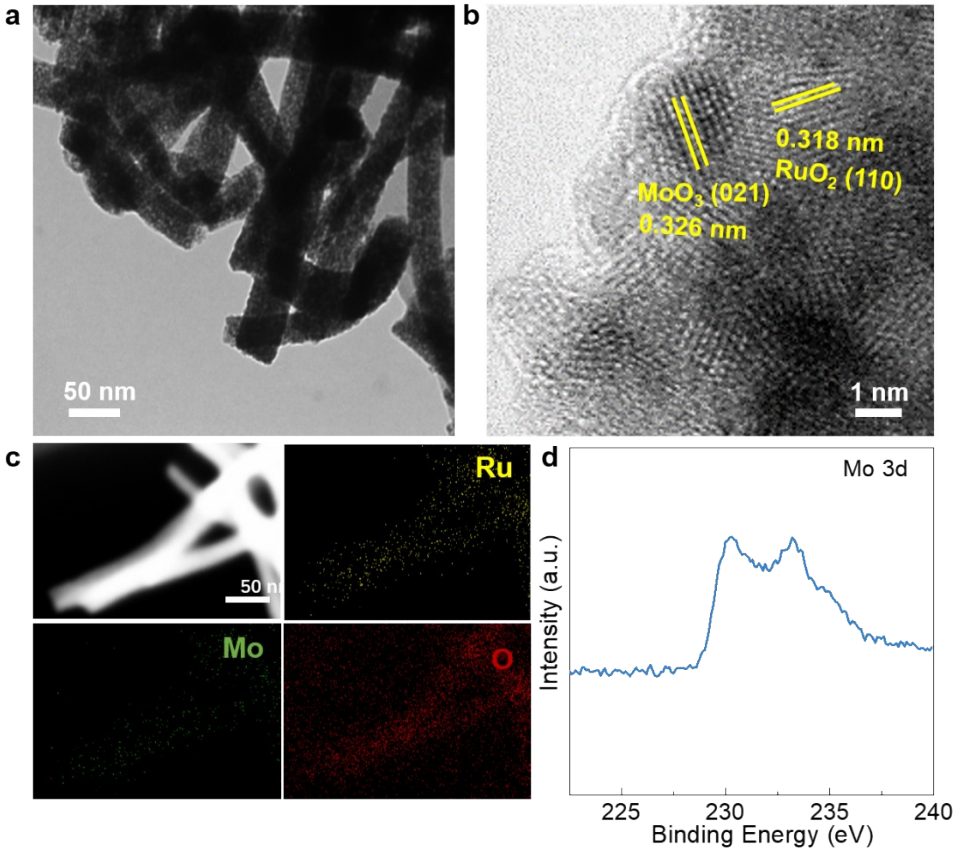


**Fig. S19.** (a) TEM image, (b) HRTEM image, (c) elemental mapping of Ru (yellow), Mo (green), and O (red) and (d) Mo 3d XPS spectrum for $RuO_2/MoO_3$ after stability test.

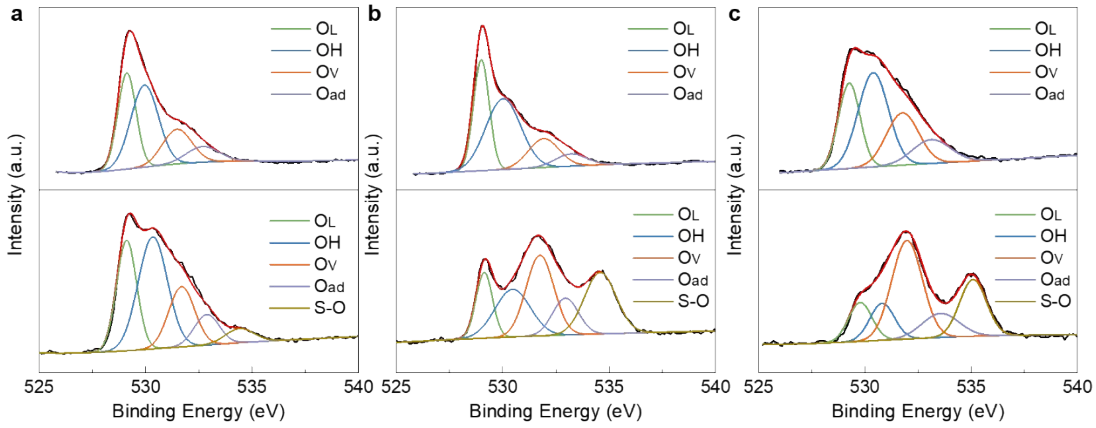


**Fig. S20.** O 1s XPS spectra of (a) $RuO_2/MoO_3$, (b) $RuO_2$, and (c) c-$RuO_2$ before and after stability test.

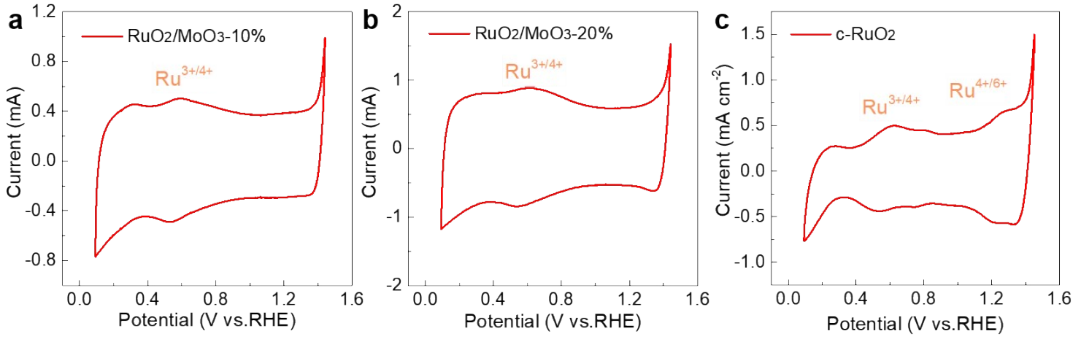


**Fig. S21.** CV curves of (a) $RuO_2/MoO_3$-10%,(b) $RuO_2/MoO_3$-20% and (c) c-$RuO_2$ measured from 0.1 to 1.45 V *vs.* RHE.

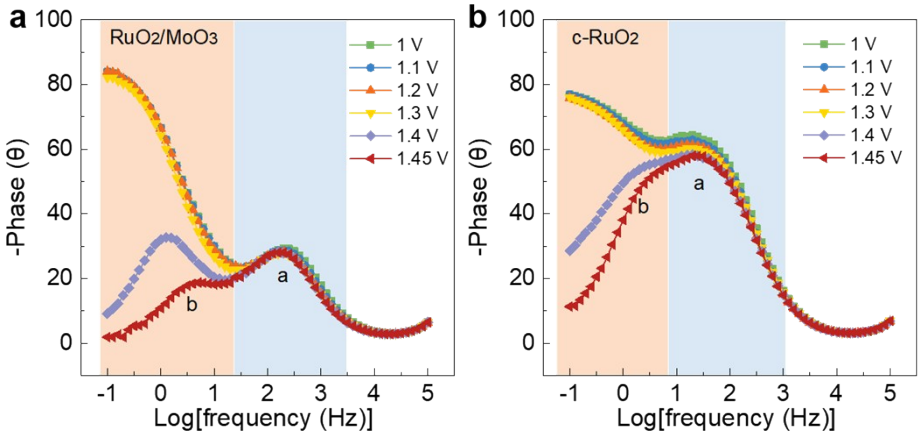


**Fig. S22.** Bode phase plots of (a) $RuO_2/MoO_3$ and (b) c-$RuO_2$.

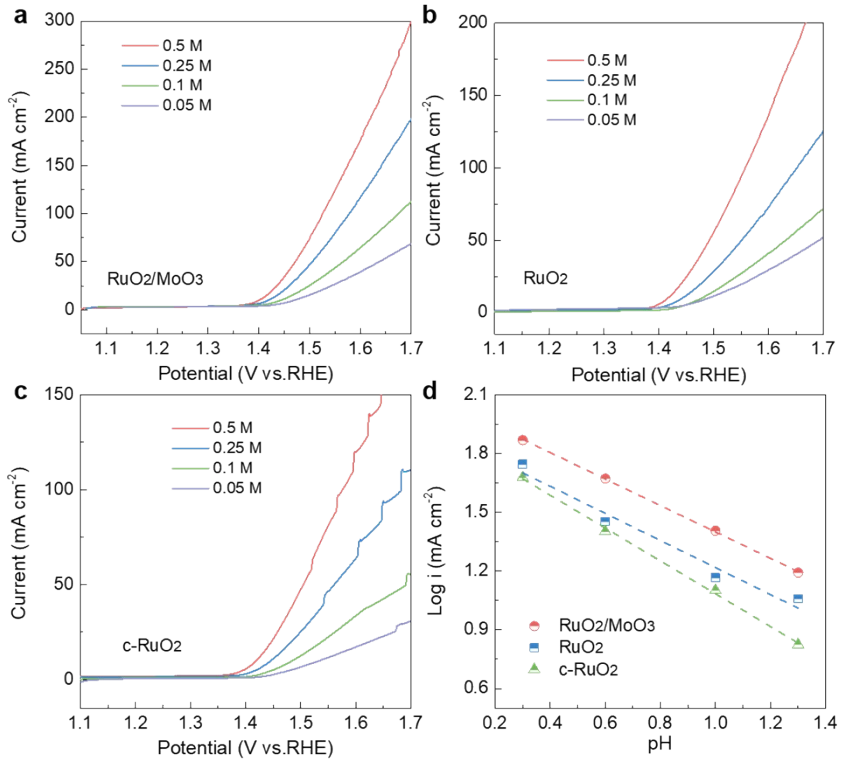


**Fig. S23.** LSV curves of (a) $RuO_2$, (b) $RuO_2$ and (c) c-$RuO_2$ in different pH values. (d) Current densities of of $RuO_2/MoO_3$, $RuO_2$, and c-$RuO_2$ catalysts at 1.5 V *vs.* RHE as a function of the pH values of electrolytes.

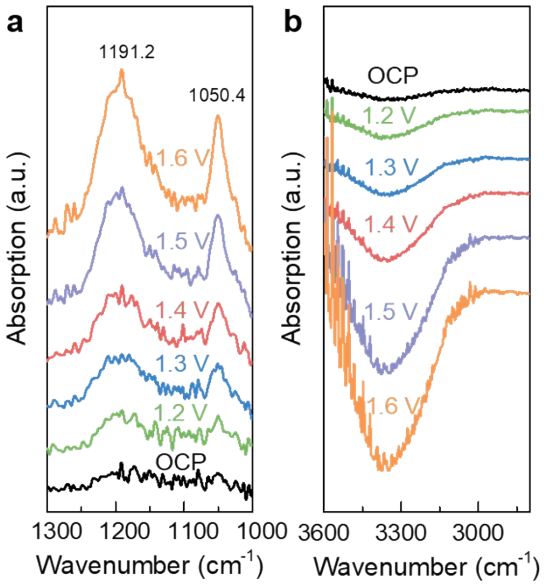


**Fig. S24.** (a) and (b) Operando FTIR spectra recorded in the potential range of 1.2-1.6 V *vs.* RHE for c-$RuO_2$.

**Table S1.** The fitted parameters of the EIS data of $RuO_2/MoO_3$, $RuO_2$, and c-$RuO_2$ catalysts recorded at an OER potential of 1.41 V (*vs.* RHE).

| Catalysts | $R_S$ (Ω) | $R_1$ (Ω) | $C_{\phi 1}$ (μF) | $n_2$ | $R_2$ (Ω) | $C_{\phi 2}$ (μF) |
|---|---|---|---|---|---|---|
| $RuO_2/MoO_3$ | 6.7 | 6.3 | 69.6 | 0.86 | 12.3 | 15.5 |
| $RuO_2$ | 6.9 | 7.3 | 94.8 | 0.89 | 19.8 | 7.9 |
| c-$RuO_2$ | 7.5 | 8.0 | 87.1 | 0.88 | 29.5 | 5.2 |

**Table S2.** Comparison of catalytic activity and stability of OER with previous literatures.

| Catalyst | Electrolyte | $\eta_{10}$ (mV) | Tafel slope (mV $dec^{-1}$) | Stability (h) | References |
|---|---|---|---|---|---|
| **$RuO_2/MoO_3$** | **0.5 M $H_2SO_4$** | **167** | **65** | **300** | **This work** |
| YZRO/AB | 0.5 M $H_2SO_4$ | 291 | 36.9 | 6 | [13] |
| 12Ru/$MnO_2$ | 0.1 M $HClO_4$ | 161 | 29.4 | 200 | [14] |
| $RuO_2$/D-$TiO_2$ | 0.5 M $H_2SO_4$ | 180 | 43 | 100 | [15] |
| YSRO-15 | 0.5 M $H_2SO_4$ | 264 | 44.8 | 28 | [16] |
| Ru@$IrO_x$ | 0.05 M $H_2SO_4$ | 282 | 69.1 | – | [17] |
| S-$RuFeO_x$ | 0.1 M $HClO_4$ | 187 | 40 | 50 | [18] |
| $RuNi_2$©G-250 | 0.5 M $H_2SO_4$ | 227 | 65 | 24 | [19] |
| PtCo-$RuO_2$/C | 0.1 M $HClO_4$ | 212.6 | 48.5 | 20 | [20] |
| Ni-$RuO_2$ | 0.1 M $HClO_4$ | 214 | 42.6 | 200 | [21] |
| $Re_{0.06}Ru_{0.94}O_2$ | 0.1 M $HClO_4$ | 190 | 45.5 | 200 | [22] |
| RuIr-NC | 0.05 M $H_2SO_4$ | 165 | – | 122 | [23] |
| $Cr_{0.6}Ru_{0.4}O_2$ | 0.5 M $H_2SO_4$ | 178 | 58 | 10 | [24] |
| RuMn NSBs-300 | 0.5 M $H_2SO_4$ | 226 | – | 122 | [25] |
| Ni-Ru@$RuO_x$-HL | 0.5 M $H_2SO_4$ | 184 | 54 | 30 | [26] |
| RuOCl@$MnO_x$ | 0.5 M $H_2SO_4$ | 228 | 43 | 280 | [27] |
| a/c-$RuO_2$ | 0.1 M $HClO_4$ | 205 | 48.6 | 60 | [28] |
| $CaCu_3Ru_4O_{12}$ | 1 M $H_2SO_4$ | 320 | 59 | – | [29] |
| RuIr@CoNC | 0.5 M $H_2SO_4$ | 223 | 45 | 40 | [30] |
| $Y_2MnRuO_7$ | 0.5 M $H_2SO_4$ | 260 | 48 | 45 | [31] |

**Table S3.** The ratios of oxygen species from XPS spectra.

| **Catalysts** | **$O_L$** | **Ru-OH** | **$O_V$** | **$O_W$** | **S-O** |
|---|---|---|---|---|---|
| $RuO_2/MoO_3$ | 31.6% | 41.0% | 18.3% | 9.1% | - |
| $RuO_2/MoO_3$-after | 26.9% | 39.9% | 19.0% | 9.2% | 5% |
| $RuO_2$ | 31.8% | 45.2% | 16.0% | 7.0% | - |
| $RuO_2$-after | 13.7% | 21.4% | 28.3% | 12.0% | 24.6% |
| c-$RuO_2$ | 25.2% | 39.3% | 23.1% | 12.4% | - |
| c-$RuO_2$-after | 12.7% | 12.5% | 41.6% | 12.3% | 20.9% |

## References


(1) X. Liang, L. Shi, Y. P. Liu, H. Chen, R. Si, W. S. Yan, Q. Zhang, G. -D. Li, L. Yang and X. X. Zou, *Angew. Chem. Int. Ed.*, 2023, **58**, 7631-7635.

(2) Y. F. Cheng, S. K. Lu, F. Liao, L. B. Liu, Y. Q. Li and M. W. Shao, *Adv. Funct. Mater.*, 2017, **27**, 1700359.

(3) C. Lin, J. -L. Li, X. P. Li, S. Yang, W. Luo, Y. J. Zhang, S. -H. Kim, D. -H. Kim, S. S. Shinde, Y. -F. Li, Z. -P. Liu, Z. Jiang and J. -H. Lee, *Nat. Catal.*, 2021, **4**, 1012-1023.

(4) L. S. Zhang, L. P. Wang, Y. Z. Wen, F. L. Ni, B. Zhang and H. S. Peng, *Adv. Mater.*, 2020, **32**, 2002297.

(5) G. Kresse and J. Hafner, *Phys. Rev. B*, 1994, **49**, 14251-14269.

(6) P. E. Blöchl, *Phys. Rev. B*, 1994, **50**, 17953-17979.

(7) J. P. Perdew and W. Yue, *Phys. Rev. B*, 1986, **33**, 8800-8802.

(8) K. Mathew, R. Sundararaman, K. Letchworth-Weaver, T. A. Arias and R. G. Hennig, *J. Chem. Phys.*, 2014, **140**, 084106.

(9) J. Rossmeisl, Z. -W. Qu, H. Zhu, G. -J. Kroes and J. K. Nørskov, *J. Electroanal. Chem.*, 2007, **607**, 83-89.

(10) V. Barone, *J. Chem. Phys.*, 2004, **120**, 3059-3065.

(11) A. A. Peterson, F. Abild-Pedersen, F. Studt, J. Rossmeisl and J. K. Nørskov, *Energy Environ. Sci.*, 2010, **3**, 1311-1315.

(12) J. K. Nørskov, J. Rossmeisl, A. Logadottir, L. Lindqvist, J. R. Kitchin, T. Bligaard and H. Jónsson, *J. Phys. Chem. B*, 2004, **108**, 17886-17892.

(13) Q. Feng, Q. Wang, Z. Zhang, Y. Y. H. Xiong, H. Y. Li, Y. Yao, X. -Z. Yuan, M. C. Williams, M. Gu, H. Chen, H. Li and H. J. Wang, *Appl. Catal. B*, 2019, **244**, 494-501.

(14) C. Lin, J. -L. Li, X. P. Li, S. Yang, W. Luo, Y. J. Zhang, S. -H. Kim D. -H., Kim, S. S. Shinde, Y. -F. Li, Z. -P. Liu, Z. Jiang and J. -H. Lee, *Nat. Catal.*, 2021, **4**, 1012-1023.

(15) X. J. Wang, X. H. Wan, X. X. Qin, C. Chen, X. S. Qian, Y. Z. Guo, Q. J. Xu, W.

-B. Cai, H. Yang and K. Jiang, *ACS Catal.*, 2022, **12**, 9437-9445.

(16) N. Zhang, C. Wang, J. W. Chen, C. Y. Hu, J. Ma, X. Deng, B. C. Qiu, L. J. Cai, Y. J. Xiong and Y. Chai, *ACS Nano*, 2021, **15**, 8537-8548.

(17) J. Q. Shan, C. X. Guo, Y. H. Zhu, S. M. Chen, L. Song, M. Jaroniec, Y. Zheng and S. -Z. Qiao, *Chem*, 2019, **5**, 445-459.

(18) Y. R. Xue, J. J. Fang, X. D. Wang, Z. Y. Xu, Y. F. Zhang, Q. Q. Lv, M. Y. Liu, W. Zhu and Z. B. Zhuang, *Adv. Funct. Mater.*, 2021, **31**, 2101405.

(19) X. J. Cui, P. J. Ren, C. Ma, J. Zhao, R. X. Chen, S. M. Chen, N. P. Rajan, H. Li, L. Yu, Z. Q. Tian and D. H. Deng, *Adv. Mater.*, 2020, **32**, 1908126.

(20) H. Jin, S. Choi, G. J. Bang, T. Kwon, H. S. Kim, S. J. Lee, Y. Hong, D. W. Lee, H. S. Park, H. Baik, Y. Jung, S. J. Yoo and K. Lee, *Energy Environ. Sci.*, 2022, **15**, 1119-1130.

(21) Z. -Y. Wu, F. -Y. Chen, B. Y. Li, S. -W. Yu, Y. Z. Finfrock, D. M. Meira, Q. -Q. Yan, P. Zhu, M. -X. Chen, T. -W. Song, Z. Y. Yin, H. -W. Liang, S. Zhang, G. F. Wang and H. T. Wang, *Nat. Mater.*, 2023, **22**, 100-108.

(22) H. Y. Jin, X. Y. Liu, P. F. An, C. Tang, H. M. Yu, Q. H. Zhang, H. -J. Peng, L. Gu, Y. Zheng, T. Song, K. Davey, U. Paik, J. Dong and S. -Z. Qiao, *Nat. Commun.*, 2023, **14**, 354.

(23) D. S. Wu, K. Kusada, S. Yoshioka, T. Yamamoto, T. Toriyama, S. Matsumura, Y. N. Chen, O. Seo, J. Kim, C. Song, S. Hiroi, O. Sakata, T. Ina, S. Kawaguchi, Y. Kubota, H. Kobayashi and H. Kitagawa, *Nat. Commun.*, 2021, **12**, 1145.

(24) Y. C. Lin, Z. Q. Tian, L. J. Zhang, J. Y. Ma, Z. Jiang, B. J. Deibert, R. X. Ge and L. Chen, *Nat. Commun.*, 2019, **10**, 162.

(25) L. G. Li, L. Z. Bu, B. L. Huang, P. T. Wang, C. Q. Shen, S. X. Bai, T. -S. Chan, Q. Shao, Z. W. Hu and X. Q. Huang, *Adv. Mater.*, 2021, **33**, 2105308.

(26) A. M. Harzandi, S. Shadman, A. S. Nissimagoudar, D. Y. Kim, H. -D. Lim, J. H. Lee, M. G. Kim, H. Y. Jeong, Y. Kim and K. S. Kim, *Adv. Energy Mater.*, 2021, **11**, 2003448.

(27) Y. X. Zhao, J. Hu, C. -L. Chiang, Y. Li, W. C. Yang, Z. H. Yang, W. -H. Hung, Y. -G. Lin, Z. Chen, B. Li, P. Q. Gao and H. Li, *J. Mater. Chem. A*, 2022, **10**, 20964-

20974.

(28) L. J. Zhang, H. Jang, H. H. Liu, M. G. Kim, D. J. Yang, S. G. Liu, X. Liu and J. Cho, *Angew. Chem. Int. Ed.*, 2021, **60**, 18821-18829.

(29) W. Liu, K. Kawano, M. Kamiko, Y. Kato, Y. Okazaki, I. Yamada and S. Yagi, *Small*, 2022, **18**, 2202439.

(30) J. Y. Xu, J. J. Li, Z. Lian, A. Araujo, Y. Li, B. Wei, Z. P. Yu, O. Bondarchuk, I. Amorim, V. Tileli, B. Li and L. F. Liu, *ACS Catal.*, 2021, **11**, 3402-3413.

(31) D. Galyamin, J. Torrero, I. Rodríguez, M. J. Kolb, P. Ferrer, L. Pascual, M. A. Salam, D. Gianolio, V. Celorrio, M. Mokhtar, D. G. Sanchez, A. S. Gago, K. A. Friedrich, M. A. Peña, J. A. Alonso, F. Calle-Vallejo, M. Retuerto and S. Rojas, *Nat. Commun.*, 2023, **14**, 2010.